Comparative Apex Electrostatics of Atom Probe Tomography Specimens

1st Qihua Zhang
School of Electrical and Computer Engineering
Georgia Institute of Technology
Atlanta, GA 30332, United States of America
+1 (206) 661-1823
kaiwah.david@gatech.edu

2nd Benjamin Klein
School of Electrical and Computer Engineering
Georgia Institute of Technology
Atlanta, GA 30332, United States of America
+1 (404) 894-2904
bklein@gatech.edu

3rd Norman A. Sanford
Quantitative Nanostructure Characterization Group
National Institute of Standards and Technology
Boulder, CO 20899, United States of America
+1 (303) 497-5239
norman.sanford@nist.gov

4th Ann N. Chiaramonti
Nanoscale Reliability Group
National Institute of Standards and Technology
Boulder, CO 20899, United States of America
+1 (303) 497-5701
chiaramonti@nist.gov

***Abstract*—Rigorous electrostatic modeling of the specimen-electrode environment is required to better understand the fundamental processes of atom probe tomography (APT) and guide the analysis of APT data. We have developed a simulation tool that self-consistently solves the nonlinear electrostatic Poisson equation along with the mobile charge carrier concentrations and provides a detailed picture of the electrostatic environment of APT specimen tips. We consider cases of metals, semiconductors, and dielectrics. Traditionally in APT, and regardless of specimen composition, the apex electric field E_{apex} has been approximated by the relation $E_{apex} = SV/(kr)$, which was originally derived for sharp, metallic conductors; we refer to this equation as the "k-factor approximation". Here, SV is tip-electrode bias, r is the radius of curvature of the tip apex, and k is a dimensionless fitting parameter with $1.5 < k < 8.5$. As expected, our Poisson solver agrees well with the k-factor approximation for metal tips; it also agrees remarkably well for semiconductor tips—regardless of the semiconductor doping level. We ascribe this finding to the fact that even if a semiconductor tip is fully depleted of majority carriers under the typical SV conditions used in APT, an inversion layer will appear at the apex surface. The inversion forms a thin, conducting layer that screens the interior of the tip —thus mimicking metallic behavior at the apex surface. By contrast, we find that the k-factor approximation applied to a purely dielectric tip results in k values far greater than the typical range for metallic tips. We put our numerical results into further context with a brief discussion of our own, separate, experimental work and the results of other publications.**

***Index Terms*—atom probe tomography, semiconductor, APT, nanoscale characterization, electrostatics, simulation**

I. Introduction

Laser-assisted atom probe tomography (APT) provides sub-nm atomic mapping of solid materials with quantitative sensitivity approaching the ppm level and is widely used to analyze the structure of materials. In APT, the specimen is biased with voltage just below the threshold for field emission of ions, while a low-power laser imparts a small thermal impulse to trigger the field evaporation process. Ion impacts are recorded on a position sensitive detector and their originating positions within the specimen can be determined, or "reconstructed", by a sequential, back-projection algorithm. A sharp, needle-like specimen is required for APT and is usually prepared in the shape of sharp spherical cap joined by a truncated cone for maximizing the electric field magnitude at the apex surface. The typical radius of curvature of the specimen apex can range from e.g. 10 nm to 70 nm [1]–[4]. Using a low-power pulsed focused laser typically with 355 nm wavelength and 2 μm beam diameter, a small thermal transient is imparted, thus triggering field emission of an ion [5]–[8]. The rate of atom evaporation R can be calculated using Arrhenius-type equation:

$$R = Ae^{\frac{-E_{act}}{k_b(T+\delta T)}} \tag{1}$$

where k_b is Boltzmann's constant, T is the specimen temperature and δT denotes the small thermal transient imparted by the pulsed laser. The activation energy E_{act} is the energy required for an ionized atom to escape from the specimen, which strongly depends on the surface electric field experienced by the atom [9]. In addition, the applied standing voltage SV influences the time-of-flight of field-evaporated atoms. Therefore, calculating the surface electric field accurately is critical to reconstructing the sample shape.

A simple analytical method was originally developed for sharp metallic conductors in the 1970s for estimating the peak electric field at the tip of a field emitter [10]. This has subsequently been applied to many types of APT specimens, not only metallic conducting specimens [11]–[13]. Using the voltage between the tip and electrode, defined as standing voltage SV, and the radius of the assumed semi-hemispherical

apex R, the electric field at the apex can be estimated using the following equation:

$$E_{apex} = \frac{SV}{kR} \tag{2}$$

where k is a dimensionless fitting parameter that depends on the geometry of the specimen and the environment [14]. For metallic specimens composed of a spherical cap atop a truncated cone, k has a range of 1.5 to 8.5 [10], [15], [16]. In this paper, we will explore whether this model is appropriate for doped semiconductor and dielectric specimen tips, using the geometry of spherical-cap, truncated-cone tips and conical-shaped local electrodes in our model and simulating the electrostatics within the APT environment. N-doped Gallium Nitride (GaN) is chosen as the semiconductor specimen, while amorphous silicon dioxide (SiO_2) is selected as the dielectric specimen. For purposes of our simulations, we assume a conical APT specimen tip is bonded to a degenerately doped Si post, which has a conical taper that matches the tip. This is illustrated in Fig. 1.

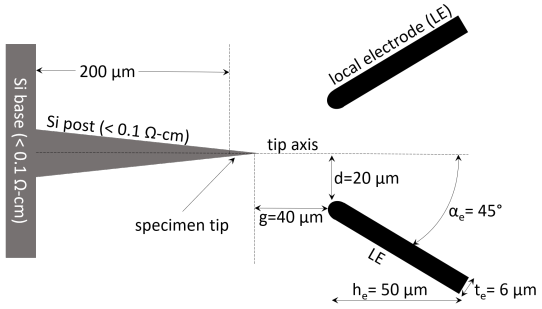

Fig. 1. Model of simplified APT environment for simulation.

II. Theory

To calculate the electrostatic potential in the APT environment, a self-consistent version of Poisson's equation for electrostatics is solved numerically. Poisson's equation in electrostatics relates the electrostatic potential ϕ to the charge densityρ, as seen in equation 3:

$$\nabla^2\phi = -\frac{\rho}{\varepsilon} \tag{3}$$

where ε denotes the electric permittivity of the medium. For a semiconductor specimen, the charge density can be found using the net charge density equation; assuming total ionization of the n-type and p-type dopant concentrations N_D and N_A, this is:

$$\rho = e(N_D - N_A + p - n) \tag{4}$$

Here n and p represent the electron and hole concentrations respectively. These carrier concentrations are calculated using the Fermi-Dirac integral containing the densities of states $g_C(E)$ and $g_V(E)$ and the Fermi distribution function $f(E)$:

$$\begin{aligned} n &= \int_{E_C(\phi)}^{+\infty} f(E)g_C(E)dE \\ &= \frac{m_n^*\sqrt{2m_n^*}}{\pi^2\hbar^3}\int_{E_C}^{+\infty}\frac{\sqrt{E-E_C(\phi)}}{1+e^{(E-E_f)/k_bT}}dE \end{aligned} \tag{5}$$

$$\begin{aligned} p &= \int_{-\infty}^{E_V(\phi)} (1-f(E))g_V(E)dE \\ &= \frac{m_p^*\sqrt{2m_p^*}}{\pi^2\hbar^3}\int_{-\infty}^{E_V}\frac{\sqrt{E_V(\phi)-E}}{1+e^{(E_f-E)/k_bT}}dE \end{aligned} \tag{6}$$

$E_C(\phi)$ and $E_V(\phi)$ are the conduction and valence band edges in the semiconductor, and are dependent on the electrostatic potential ϕ:

$$E_C(\phi) = E_{C,0} - e\phi \tag{7}$$

$$E_V(\phi) = E_{V,0} - e\phi \tag{8}$$

where $E_{C,0}$ and $E_{V,0}$ refer to the conduction and valence band edges under no applied bias. Assembling the equations above, we can rewrite Poisson's equation and show explicitly that both the left-hand side and the right-hand side are dependent upon the electrostatic potential, thus requiring a self-consistent solution:

$$\begin{aligned} \frac{\varepsilon}{e}(\nabla^2\cdot\phi) = N_D - N_A \\ + \frac{m_p^*\sqrt{2m_p^*}}{\pi^2\hbar^3}\int_{-\infty}^{E_{V,0}-e\phi}\frac{\sqrt{E_V(\phi)-E}}{1+e^{(E_f-E)/k_bT}}dE \\ - \frac{m_n^*\sqrt{2m_n^*}}{\pi^2\hbar^3}\int_{E_{C,0}-e\phi}^{+\infty}\frac{\sqrt{E-E_C(\phi)}}{1+e^{(E-E_f)/k_bT}}dE. \end{aligned} \tag{9}$$

The self-consistent Poisson's equation is discretized and solved in Matlab [1] as will be described briefly below.

III. Simulation Modeling

In order to create an accurate model to solve for the electrostatic potential and fields in the tip-electrode environment, a 3D cylindrically-symmetric model with the tip axis as the left boundary is designed and discretized via meshing of the interior regions. The model is a combination of three parts: the specimen tip, local electrode, and the essential boundaries.

A. Tip Modeling

The half-specimen tip is modeled as a quarter circle with one end expanding at a given angle. Fig. 2 shows the modeled specimen half-tip of $0.02\ \mu m$ radius and 5° half-expansion angle. The enclosed area is assigned the material properties of the specimen (n-doped GaN or SiO_2). For n-doped GaN at temperature $T = 50\ K$, we used a bandgap energy of $3.437eV$ and a relative dielectric constant of $\varepsilon_{GaN} = 8.9$ [17], [18]. For SiO_2 at the same temperature, we assumed zero fixed and mobile charge, and used a relative dielectric constant of $\varepsilon_{SiO_2} = 3.78$ [19].

[1]Any mention of commercial products is for information only; it does not imply recommendation or endorsement by NIST.

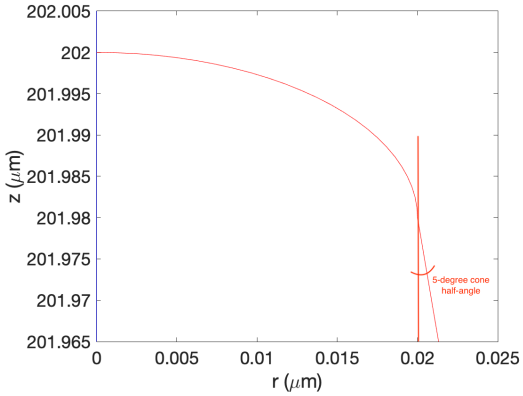

Fig. 2. Specimen half-tip in tip-electrode environment.

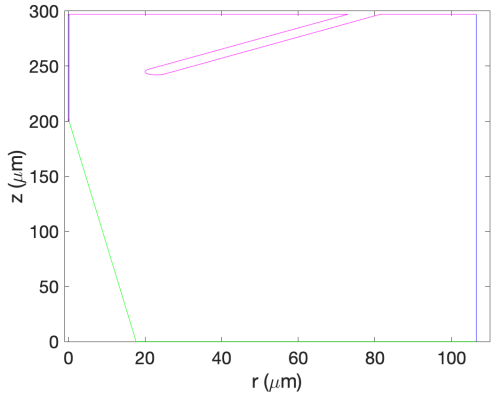

Fig. 3. Cross-sectional View of tip-electrode environment. The pink lines represent the top Dirichlet boundary, including the local electrode. The green lines represent the bottom Dirichlet boundary, including the Si post. The blue line represents a von Neumann boundary.

B. Local Electrode (LE)

The local electrode creates the highly localized electric field necessary for field evaporation. The ion passes through the hollow conical local electrode (LE) on its way to the detector. Referring to Fig. 1, the tip and LE are rotationally symmetric around a common z-axis. Our representative LE dimensions are adapted from Bajikar *et al.* [20]. The LE is modeled as a truncated cone with an open aperture radius of $d = 20\ \mu m$ facing the specimen tip. The tip-electrode separation $g = 40\ \mu m$. The electrode wall thickness $t_e = 6\ \mu m$, but choosing $t_e = 2\mu m$ as mentioned in Bajikar *et al.* does not substantially change the computed results. The radius of curvature of the electrode edge facing the specimen tip is $t_e/2$. The LE is modeled as part of the top Dirichlet boundary (a boundary which is held at a constant electrostatic potential along its entire spatial extent) and given a potential equal to SV.

C. Boundaries

Apart from the top Dirichlet boundary including the local electrode mentioned above, another Dirichlet boundary is formed at the bottom of the simulated region, which represents the Si post directly connected to the specimen tip. The Si post is degenerately doped and assumed to be grounded. The two Dirichlet boundaries are used as the biasing contacts. Fig. 3 shows a cross-sectional model of the APT. Von Neumann boundaries (a boundary on which the normal component of the electric field is forced to be zero) are placed on the left and right side of the model to enclose the modelled region. The left von Neumann boundary represents the cylindrical axis of symmetry. In this model, the area enclosed by the outer simulation boundaries and the outer edge of the specimen tip is vacuum. We neglect the residual ions in the vacuum, which do not significantly influence the experimental results for the measurements being modeled here.

D. Model Meshing

Discretizing Poisson's equation requires a mesh covering the simulated regions. To create the mesh, we used the 'Triangle' program developed by Shewchuk for Delaunay triangular mesh generation [21], [22]. Shown below are four figures showing the original model and the meshed results: The

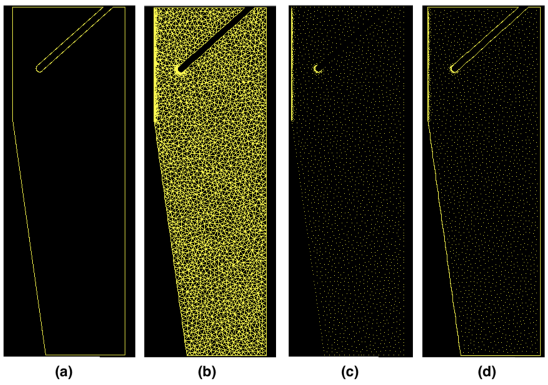

Fig. 4. Figures showing meshed results after executing Triangle program. Fig. (a) is the model before meshing; Fig. (b) shows the model after meshing; Fig. (c) displays all the nodes/vertices; Fig. (d) displays the nodes under the boundary edges.

half tip-electrode model regions are subdivided into meshing triangles, seen in Fig.4. Regions in which the electrostatic potential is expected to vary rapidly are set to have greater mesh refinement, and the overall refinement is increased until the results converge. Poisson's equation is discretized on this mesh using the finite volume method [23]. An in-house Poisson's solver has been developed, which uses the Newton-Raphson method to update the electrostatic potential on each mesh node, and iterate until the solution error falls below a designated threshold [24]. Once the electrostatic potential at each node is obtained, the electric field can be calculated by using the finite difference approximation to estimate the gradient of the electrostatic potential.

IV. Results and Analysis

A. Semiconductor Specimens

High SVs are one of the conditions to trigger field evaporation of atoms given the radii of the specimen tips that are able to be easily fabricated by focused ion beam milling. The first example presented is an unintentionally n-doped semiconductor GaN tip specimen with an apex radius of 20 nm at $SV = 2\ kV$ applied between the two biasing contacts. The electron concentration for an unintentionally-doped GaN is 1e16 cm^{-3} [25]. A 2 kV SV is a typical onset voltage of field evaporation for GaN tip of this radius, making it a representative case to model. A contour plot showing the electrostatic potential levels in the area surrounding the tip is shown in fig.5. As expected, the contour lines are denser

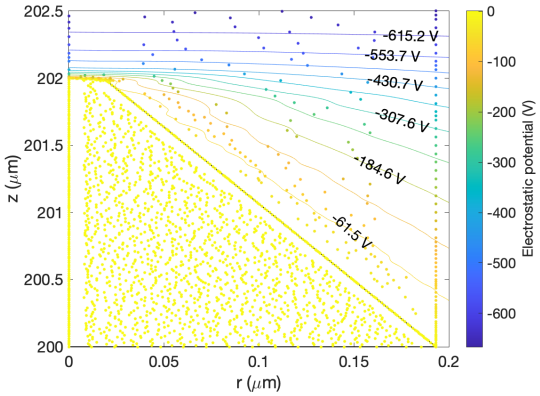

Fig. 5. Contour plot of electrostatic potential levels surrounding the tip area. (GaN, $T = 50\ K$, $r = 20\ nm$, $N_D = 1e16\ cm^{-3}$, $SV = 2\ kV$)

near the tip apex, showing that the electrostatic potential varies most rapidly in this region. The electric field along the tip axis ($r = 0\ \mu m$) is calculated and plotted, as shown in Fig. 6. A

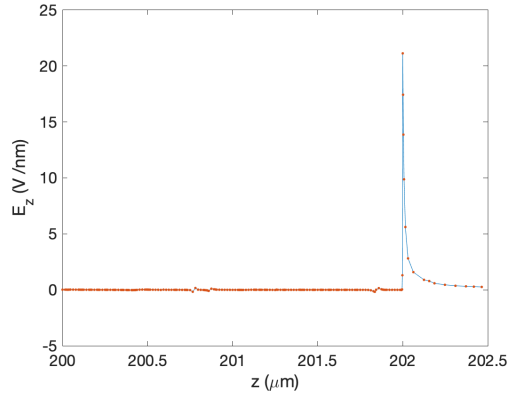

Fig. 6. Electric field on the Tip Axis. (GaN, $T = 50\ K$, $r = 20\ nm$, $N_D = 1e16\ cm^{-3}$, $SV = 2\ kV$)

sharp peak of electric field magnitude of 21 V/nm can be observed at the tip apex($z = 202\ \mu m$).

This simulation was repeated for a range of specimen tips. Another simulation is shown below for GaN tip with an apex radius of 200 nm with the other simulation parameters unchanged. The contour plot shown in Fig. 7 again shows

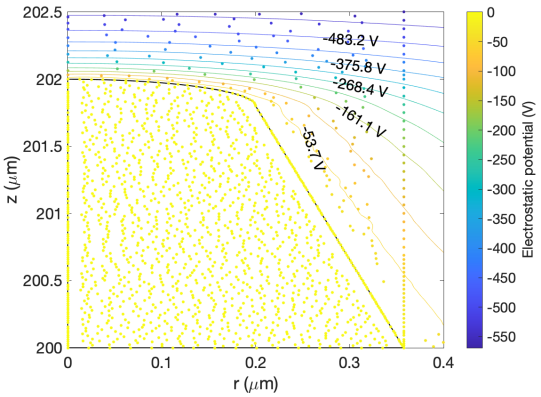

Fig. 7. Contour plot of electrostatic potential levels surrounding the tip area. (GaN, $T = 50\ K$, $r = 200\ nm$, $N_D = 1e16\ cm^{-3}$, $SV = 2\ kV$)

a rapidly changing electrostatic potential near the tip apex. Compared to the previous example, the rate of change in electrostatic potential is less in the same region due to the larger radius tip, but the position where the peak of electric field along the tip axis occurs remains unchanged. As shown in Fig.8, the peak electric field occurs at $z = 202\ \mu m$ with a magnitude of 3 V/nm. The 2 kV bias case is chosen only to

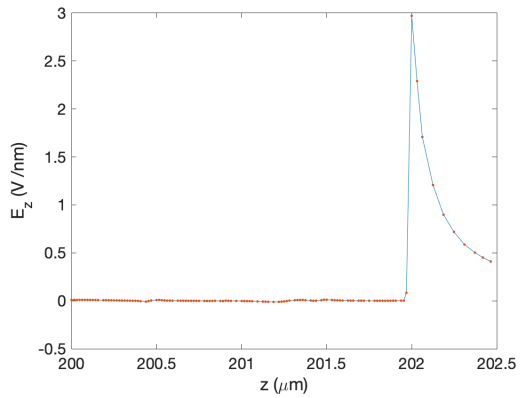

Fig. 8. Electric field on the Tip Axis. (GaN, $T = 50\ K$, $r = 200\ nm$, $N_D = 1e16\ cm^{-3}$, $SV = 2\ kV$)

compare the result with the prior example, which illustrated a tip with a much smaller apex radius. For this 200 nm apex radius case, a surface field of 3 V/nm would not likely yield ionic field emission. Indeed, as shown in Ref. [26], GaN specimen tips with apex radii of roughly 100 nm are usually run with SV in the range of 8 kV to 10 kV; this hypothetical example with an apex radius of 200nm would require an even higher SV.

Applying the k factor approximation model described in the Introduction, we can calculate the k parameter by using the apex electric field, SV and tip radius. We have simulated multiple SV cases ranging from 2 kV to 10 kV and calculated

the resulting apex electric field and k factor. Fig. 9 shows the distribution of k factor for both example cases. Surprisingly,

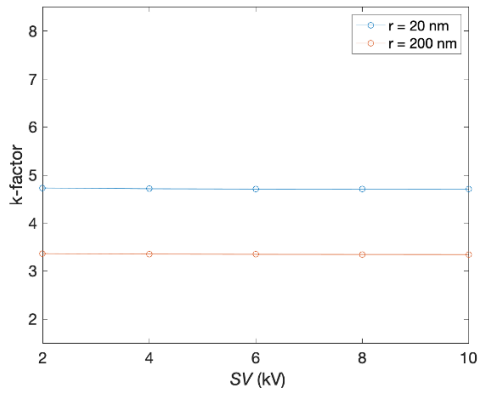

Fig. 9. k factor for both example cases. (GaN, $T = 50\ K$, $N_D = 1\text{e}16\ cm^{-3}$, $SV = 2 - 10\ kV$)

k factor for both GaN tips is within the typical range for metal tips, $1.5 - 8.5$. Both GaN tips seem to have 'metal-like' behavior in the APT environment as demonstrated by conformance to the Birdseye approximation for metals.

To better understand the metal-like behavior of the GaN specimens, a study of the charge density distribution within the tip was performed. As the fixed charge density (ionized dopants) only depends on doping concentration within the semiconductor tip, a plot of mobile charge density distribution is most instructive. Fig. 10 shows a scatter plot of mobile charge density within the tip of the first example case. The ma-

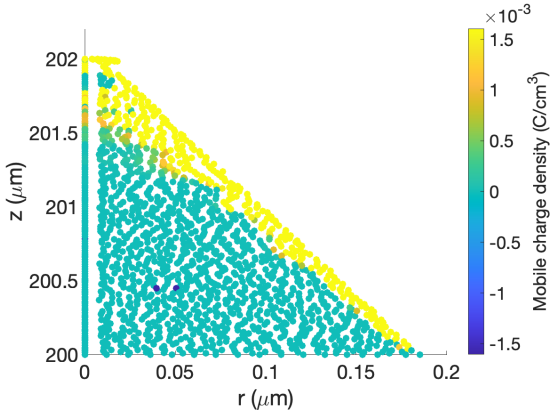

Fig. 10. Scatter plot mobile charge density within the specimen tip. (GaN, $T = 50\ K$, $r = 20\ nm$, $N_D = 1\text{e}16\ cm^{-3}$, $SV = 2\ kV$)

jority carriers (electrons) within the n-doped tip, represented in purple, have been entirely depleted due to the applied SV. An inversion layer of positive charge carriers (holes) appears at the apex surface and the nearby outer edge. The charge inversion forms a thin, p-type conducting layer that screens the interior of the tip, thus mimicking metallic behavior at the specimen surface.

In addition, a series of figures showing the depletion of majority carriers and formation of an inversion layer are presented in Fig. 11, where SV ranges from 20 V to 40 V. The inversion layer occurs at the tip apex even at $SV = 20\ V$,

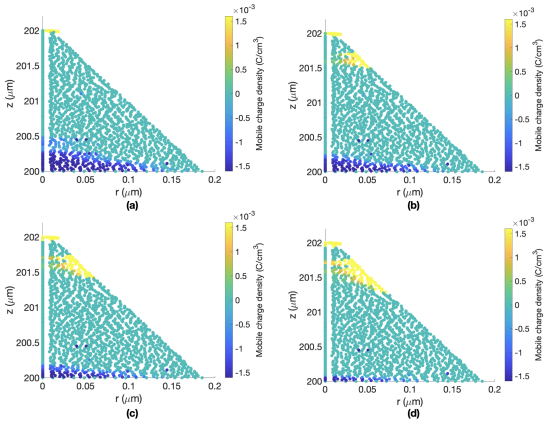

Fig. 11. Scatter plots mobile charge density at low SVs. (GaN, $T = 50\ K$, $r = 20\ nm$, $N_D = 1\text{e}16\ cm^{-3}$, $SV =$ (a) 20 V; (b)25 V; (c)30 V; (d) 40 V)

where a large portion of majority carriers have already been depleted. As SV increases, a second inversion layer appears. For $SV = 40\ V$, majority carriers are nearly depleted and the inversion region increases.

B. Sensitivity of Results to Model Parameters

The apex electric field E_{apex} depends upon variations in tip and electrode geometry as well as specimen doping concentration. As mentioned in the previous section, varying the LE wall thickness t_e (from 2 μm to 6 μm) has negligible effect on the apex field. However, a 10-fold increase in apex radius r of the specimen tip (from 20 nm to 200 nm) results in a reduction in E_{apex} by 7 times (from $\sim$ 21 V/nm to $\sim$ 3 V/nm). Further simulations have shown that reducing the vertical length of Si-post by half (from 200 μm to 100 μm) results in a 5.8% reduction in E_{apex} (from 21.13 V/nm to 19.89 V/nm). In addition, a 5-degree decrease in half-tilted angle α_e of the LE (from 45° to 40°) results in 2% drop in E_{apex} (from 21.13 V/nm to 20.71 V/nm). An increase in n-type doping concentration N_D by a factor of 100 (from 1e16 cm^{-3} to 1e18 cm^{-3}) raises E_{apex} by 17% (from 21.13 V/nm to 24.75 V/nm).

C. Dielectrics

While the apex regions of semiconductor specimen tips exhibit metal-like behavior and and may be adequately represented using the k factor approximation, insulating dielectric specimens produce k factors which fall far outside the normal range for metallic samples. Shown below is an on-axis electric field plot with amorphous silicon dioxide SiO_2 as the tip specimen. Except for the material composition and dielectric constant of the tip, all other simulation parameters are the same as for the first example case above. Compared to the on-axis electric field of the GaN tip in Fig. 6, several differences can be observed between these cases. First, the maximum electric field strength in the amorphous SiO_2 tip case occurs at the

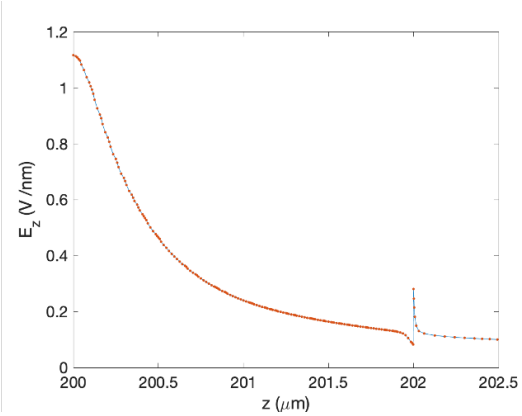

Fig. 12. Electric field on the Tip Axis. (SiO_2, $T = 50\ K$, $r = 20\ nm$, $SV = 2\ kV$)

base of the tip, while that in the GaN tip occurs at the apex of the tip. Second, although a spike in electric field can be seen at the SiO_2 tip apex, the magnitude of this spike is small compared to the magnitude of the peak which occurs at the base. Overall, the magnitude of electric field at the apex tip in the amorphous SiO_2 case is significantly smaller than that in the GaN case. The effective k factor in the amorphous SiO_2 case is much larger than for GaN, and the resulting k value is far outside of the typical range for metallic tips. It may be more appropriate to use the parameters of the conducting silicon post in the k-factor approximation in this case, as the peak field occurs at the base of the dielectric and the apex of the Si post.

The $SV = 2\ kV$ case just discussed should roughly conform to a bias regime whereby the induced electric field strength within the amorphous SiO_2 tip is near or below the dielectric breakdown for fused silica [27]. In practice, however, we find that SiO_2 tips of similar apex configuration tend to run in APT with SV in the range of $5\ kV$ to $7\ kV$. Moreover, such APT runs will often display artifacts, which appear to be correlated with photoconductive, electrostatic, and/or transient dielectric conductivity [28]. Clearly, establishing a reliable and rigorous microscopic theory of APT for dielectric specimens is a challenging undertaking, but attempts to attack the problem (at least for dielectric MgO) have been presented [29].

V. Conclusion

We have conducted comparative simulation studies on doped semiconductor specimens of various tip radii, as well as dielectric specimens, in the APT environment. We found that uniform semiconductor APT tips have apex electrostatic behavior similar to that of metallic tips, regardless of tip radius, and the k factor apex field approximation developed for metallic tips is also appropriate for semiconductor GaN tips. The charged inversion layer induced by high fields at the outer edge of the tip and apex surface is responsible for effective metallic behavior of semiconductor atom probe tips. On the other hand, due to its inability to form an inversion layer of charges, the k factor for insulating dielectric specimens falls far outside the range used for metallic tips. We calculated a weak electric field strength at the tip apex compared to the base of the tip in dielectric specimens. Future studies will investigate the behavior of multi-layer structures such as metal/semiconductor/dielectric specimens, which require careful electrostatic simulation of the type developed in this paper.

Acknowledgment

The authors acknowledge generous support from NIST.

Conflict of Interest

The authors declare no conflict of interest.

References

[1] W. Chen and P. Pareige, "11 - using atom probe tomography in the study of semiconductor nanowires," in *Semiconductor Nanowires* (J. Arbiol and Q. Xiong, eds.), Woodhead Publishing Series in Electronic and Optical Materials, pp. 305 – 326, Woodhead Publishing, 2015.

[2] C. Kong, S. Cheong, and R. D. Tilley, "2.15 - recent development in focused ion beam nanofabrication," in *Comprehensive Nanoscience and Nanotechnology (Second Edition)* (D. L. Andrews, R. H. Lipson, and T. Nann, eds.), pp. 327 – 356, Oxford: Academic Press, second edition ed., 2019.

[3] R. Kohli, "Chapter 5 - developments in imaging and analysis techniques for micro- and nanosize particles and surface features," in *Developments in Surface Contamination and Cleaning* (R. Kohli and K. Mittal, eds.), pp. 215 – 306, Oxford: William Andrew Publishing, 2012.

[4] X. Wang, C. Hatzoglou, B. Sneed, Z. Fan, W. Guo, K. Jin, D. Chen, H. Bei, Y. Wang, W. J. Weber, Y. Zhang, B. Gault, K. L. More, F. Vurpillot, and J. D. Poplawsky, "Interpreting nanovoids in atom probe tomography data for accurate local compositional measurements," *Nature Communications*, vol. 11, p. 1022, Feb 2020.

[5] M. D. Mulholland and D. N. Seidman, "Voltage-pulsed and laser-pulsed atom probe tomography of a multiphase high-strength low-carbon steel," *Microscopy and Microanalysis*, vol. 17, no. 6, p. 950–962, 2011.

[6] J. H. Bunton, J. D. Olson, D. R. Lenz, and T. F. Kelly, "Advances in pulsed-laser atom probe: Instrument and specimen design for optimum performance," *Microscopy and Microanalysis*, vol. 13, no. 6, p. 418–427, 2007.

[7] G. L. Kellogg and T. T. Tsong, "Pulsed-laser atom-probe field-ion microscopy," *Journal of Applied Physics*, vol. 51, no. 2, pp. 1184–1193, 1980.

[8] M. Gilbert, F. Vurpillot, A. Vella, H. Bernas, and B. Deconihout, "Some aspects of the silicon behaviour under femtosecond pulsed laser field evaporation," *Ultramicroscopy*, vol. 107, no. 9, pp. 767 – 772, 2007.

[9] M. K. Miller and R. G. Forbes, *Field Evaporation and Related Topics*, pp. 111–187. Boston, MA: Springer US, 2014.

[10] P. J. Birdseye and D. Smith, "The electric field and the stress on a field-ion specimen," *Surface Science*, vol. 23, no. 1, pp. 198 – 210, 1970.

[11] T. F. Kelly, *Atom-Probe Tomography*, pp. 2–2. Cham: Springer International Publishing, 2019.

[12] R. Gomer, "Field emission, field ionization, and field desorption," *Surface Science*, vol. 299-300, pp. 129 – 152, 1994.

[13] A. Cerezo, P. H. Clifton, M. J. Galtrey, C. J. Humphreys, T. F. Kelly, D. J. Larson, S. Lozano-Perez, E. A. Marquis, R. A. Oliver, G. Sha, K. Thompson, M. Zandbergen, and R. L. Alvis, "Atom probe tomography today," *Materials Today*, vol. 10, no. 12, pp. 36 – 42, 2007.

[14] S. M. Reddy, D. W. Saxey, W. D. A. Rickard, D. Fougerouse, S. D. Montalvo, R. Verberne, and A. van Riessen, "Atom probe tomography: Development and application to the geosciences," *Geostandards and Geoanalytical Research*, vol. 44, no. 1, pp. 5–50, 2020.

[15] T. F. Kelly, P. P. Camus, D. J. Larson, L. M. Holzman, and S. S. Bajikar, "On the many advantages of local-electrode atom probes," *Ultramicroscopy*, vol. 62, no. 1, pp. 29 – 42, 1996.

[16] S. T. Loi, B. Gault, S. P. Ringer, D. J. Larson, and B. P. Geiser, "Electrostatic simulations of a local electrode atom probe: The dependence of tomographic reconstruction parameters on specimen and microscope geometry," *Ultramicroscopy*, vol. 132, pp. 107 – 113, 2013.

[17] O. Madelung, *Physical data*, pp. 5–159. Berlin, Heidelberg: Springer Berlin Heidelberg, 1991.
[18] E. F. Schubert, *Light-Emitting Diodes*. Cambridge University Press, 2 ed., 2006.
[19] B. El-Kareh, *Thermal Oxidation and Nitridation*, pp. 39–85. Boston, MA: Springer US, 1995.
[20] S. S. Bajikar, T. F. Kelly, and P. P. Camus, "Electrostatic analysis of local-electrode atom probes," *Applied Surface Science*, vol. 94-95, pp. 464 – 471, 1996. Proceedings of the 42nd International Field Emission Symposium.
[21] J. R. Shewchuk, "Delaunay refinement algorithms for triangular mesh generation," *Computational Geometry*, vol. 22, no. 1, pp. 21 – 74, 2002. 16th ACM Symposium on Computational Geometry.
[22] J. R. Shewchuk, "Triangle: Engineering a 2D Quality Mesh Generator and Delaunay Triangulator," in *Applied Computational Geometry: Towards Geometric Engineering*, vol. 1148 of *Lecture Notes in Computer Science*, pp. 203–222, Springer-Verlag, 5 1996.
[23] Z.-C. Li and S. Wang, "The finite volume method and application in combinations," *Journal of Computational and Applied Mathematics*, vol. 106, no. 1, pp. 21 – 53, 1999.
[24] T. Dence, "Cubics, chaos and newton's method," *The Mathematical Gazette*, vol. 81, no. 492, pp. 403–408, 1997.
[25] K. Ueno, A. Kobayashi, and H. Fujioka, "Characteristics of unintentionally doped and lightly si-doped gan prepared via pulsed sputtering," *AIP Advances*, vol. 9, no. 7, p. 075123, 2019.
[26] N. A. Sanford, P. T. Blanchard, M. Brubaker, K. A. Bertness, A. Roshko, J. B. Schlager, R. Kirchhofer, D. R. Diercks, and B. Gorman, "Laser-assisted atom probe tomography of mbe grown gan nanowire heterostructures," *physica status solidi c*, vol. 11, no. 3-4, pp. 608–612, 2014.
[27] J. Ruzyllo, *silicon dioxide,* SiO_2. World Scientific, 2016.
[28] B. W. Caplins, P. T. Blanchard, A. N. Chiaramonti, D. R. Diercks, L. Miaja-Avila, and N. A. Sanford, "An algorithm for correcting systematic energy deficits in the atom probe mass spectra of insulating samples," *Ultramicroscopy*, vol. 213, p. 112995, June 2020.
[29] E. P. Silaeva, L. Arnoldi, M. L. Karahka, B. Deconihout, A. Menand, H. J. Kreuzer, and A. Vella, "Do dielectric nanostructures turn metallic in high-electric dc fields?," *Nano Letters*, vol. 14, no. 11, pp. 6066–6072, 2014.